

## PAPER

View Article Online  
View Journal | View IssueCite this: *Digital Discovery*, 2023, 2, 1070

## Highly transferable atomistic machine-learning potentials from curated and compact datasets across the periodic table†

Christopher M. Andolina <sup>a</sup> and Wissam A. Saidi <sup>\*ab</sup>

Machine learning atomistic potentials trained using density functional theory (DFT) datasets allow for the modeling of complex material properties with near-DFT accuracy while imposing a fraction of its computational cost. The curation of the DFT datasets can be extensive in size and time-consuming to train and refine. In this study, we focus on addressing these barriers by developing minimalistic and flexible datasets for many elements in the periodic table regardless of their mass, electronic configuration, and ground state lattice. These DFT datasets have, on average, ~4000 different structures and 27 atoms per structure, which we found sufficient to maintain the predictive accuracy of DFT properties and notably with high transferability. We envision these highly curated training sets as starting points for the community to expand, modify, or use with other machine learning atomistic potential models, whatever may suit individual needs, further accelerating the utilization of machine learning as a tool for material design and discovery.

Received 18th March 2023

Accepted 18th June 2023

DOI: 10.1039/d3dd00046j

rsc.li/digitaldiscovery

## 1. Introduction

Numerous studies on code the development, training, validation, and transferability of machine learning atomistic potentials (MLPs) have recently been reported, highlighting notable and significant advances in materials modeling.<sup>1–4</sup> Many of these studies underscore that MLPs have high fidelity in simulating various properties and are significantly less computationally demanding than density functional theory (DFT) calculations.<sup>4</sup> Therefore, MLPs can readily be used to model known materials at large sizes (a recent study claiming ten billion atoms<sup>5</sup>) and long timescales and to discover the applications of interest,<sup>6</sup> further accelerating the computational modeling of materials.<sup>7</sup> Recent refinements of machine learning (ML) approaches<sup>8,9</sup> and training methodologies<sup>7,10</sup> have further improved the accuracy, precision, and utility of these atomistic potentials and their use for various material applications.<sup>11</sup> Computational material science has seized the development of these ML advances for chemical modeling applications<sup>12</sup> and applied them to describe complex dynamic

systems, including single elementals,<sup>13</sup> bimetallic systems,<sup>14–16</sup> supported metal nanoclusters,<sup>17</sup> hybrid perovskites,<sup>18</sup> and metal oxides.<sup>19</sup> Although MLPs, in general, are less time-consuming to train/refine and more robust at describing systems outside of their training datasets (transferability)<sup>20–23</sup> compared to classical atomistic potentials (*e.g.*, embedded atom model potentials), the training workflow and database composition are areas that could benefit from further optimization, as noted in current reviews in literature.<sup>24,25</sup>

We aim to further advance MLP development by providing a clear and systematic approach to curating minimalistic DFT datasets that can be applied to almost any element in the periodic table (Fig. 1). Creating databases to train ML potentials is a challenging endeavor regardless of the ultimate application of the atomistic potential.<sup>26</sup> This study focuses on using deep

<sup>a</sup>Department of Mechanical Engineering and Materials Science, University of Pittsburgh, Pittsburgh, PA 15261, USA. E-mail: alsaidi@pitt.edu

<sup>b</sup>National Energy Technology Laboratory, United States Department of Energy, Pittsburgh, PA 15236, USA

† Electronic supplementary information (ESI) available: Details for all DNP and DFT values for each lattice, point defect, elastic constant, and surface that was presented in the plots. As well as configuration counts for the training data. DFT training data, DNPs, and example validation scripts can be found here (<https://github.com/saidigroup/23-Single-Element-DNPs>). See DOI: <https://doi.org/10.1039/d3dd00046j>

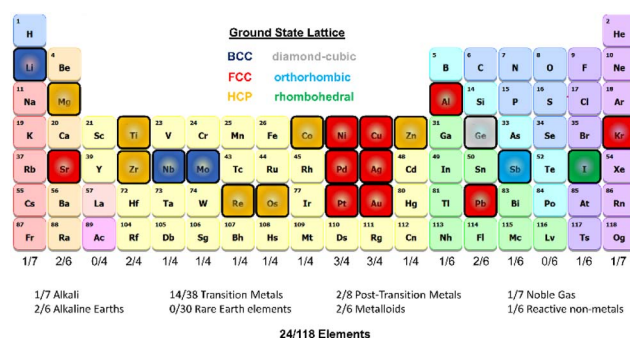


Fig. 1 Schematic of the period table visualizing the elements selected for this work and highlighting the ground state lattice configurations.



neural network models to develop atomistic potentials. Although we specifically examine the predictive accuracy of the deep neural network potentials (DNP) with these DFT datasets, we expect other MLP models to have a similar accuracy based on prior investigations.<sup>27</sup> We note there are few examples of these highly applicable methodologies for multiple (over 23) elements,<sup>28</sup> which are distinct from this approach and rely on an automated workflow (DP-GEN).<sup>29</sup>

We demonstrate our approach by sampling elements with distinct masses, electron configurations, and ground-state crystal phases (excluding rare earth elements). Our method for developing single-element datasets depends on the curated Material Project database (MPDB)<sup>30</sup> and the NOMAD repository and archive,<sup>31</sup> and a DeePMD-kit neural network approach.<sup>32</sup> We refine our DNP models using adaptive learning. We apply an ensemble approach to compare single-element inter-DNP deviations of randomly seeded models and select configurations with more significant force deviations for further training. The final single-element potentials were trained for up to three iterations, containing less than  $3857 \pm 1032$  with an overall average of  $27 \pm 12$  atoms per structure (see Table S1 for more details†). These DNPs can accurately predict several properties of five low-energy lattice configurations for each element. As shown below, the resulting potentials have good transferability to atomic environments not explicitly included in the training database (e.g., other lattice configurations, vacancies, surfaces, and the thermal stability of the solid phase).

## 2. Computational methods

### 2.1 Curation of the DFT dataset for DNP training

Initial DFT parent structures comprise five of the lowest energy lattice structures deposited in MPDB<sup>33</sup> (e.g., face-center-cubic (fcc), body-center-cubic (bcc), hexagonal, hexagonal close-pack (hcp), rhombohedral, orthogonal, tetragonal, trigonal, simple cubic, and/or diamond cubic). If five structures were not located in the MPDB for a select element, additional lattice crystal systems were obtained from the NOMAD Repository and Archive<sup>31</sup> or generated<sup>34</sup> and optimized using DFT (VASP)<sup>35–37</sup> before training. The specific lattices used for training vary from element to element; the ESI† provides a complete list of phases (Table S2†). Generally, for the ground state configuration, single-point defect structures (vacancy Table S4† or interstitial Table S5†) were generated from a DFT-optimized  $2 \times 2 \times 2$  supercell of the conventional lattice structure. Additionally, each dataset contained a set of deformed lattices in twelve directions, typically employed to calculate elastic constants from finite differences. For each parent structure (point defect type and each of the 12 deformed lattices), 20 configurations were generated from a molecular dynamics (MD) trajectory with constant volume and temperature (NVT) at two temperatures ( $T_m$  and  $0.25 T_m$ ) for the elements with melting temperatures  $T_m$  at  $<2000$  K, and three temperatures ( $T_m$ ,  $0.6 T_m$ , and  $0.25 T_m$ ) for selected elements with  $T_m > 2000$  K.

The VASP calculations were performed using the Perdew–Burke–Ernzerhof (PBE) exchange–correlation functional with projector-augmented wave pseudopotentials,<sup>35–37</sup> which

correspond to those used by the corresponding elements listed in the MPDB.<sup>33,38</sup> We selected a plane-wave cut-off of 400 eV that was used consistently across all materials. We used a tight break condition of  $10^{-8}$  eV free energy change between steps in the electronic relaxation loop. Moreover, we applied Methfessel–Paxton<sup>39</sup> smearing of 2<sup>nd</sup>-order with 0.15 eV, broadening to sample the Brillouin zone. We used a  $k$ -spacing value of  $0.24 \text{ \AA}^{-1}$  for all calculations, which we previously showed to be sufficient for training purposes; the DNPs generated using the DFT training database were found to be less sensitive to errors from under-sampling the Brillouin zone than the standard DFT calculations.<sup>13</sup>

### 2.2 Description of the DNP training procedure

Machine learning potentials were trained using the DeePMD-kit (v2.1.2)<sup>40</sup> within the DeepPot-SE<sup>41</sup> approach. The DeePMD-kit utilizes neural networks to interpolate the relationship between atomic coordinates (model input samples) and energies, forces, and virials (model output labels) in the DFT training data. We used a consistent training protocol with identical hyperparameters for each DNP, including randomly initialized weights in the neural networks. The complete set of hyperparameters used for training is provided in a DeePMD-kit input file in the ESI†.

Three DNPs with initial randomized weights were generated at each step of the iterative training process. LAMMPS was utilized to calculate various properties (*vide infra*) for each element. The averages and standard deviations of the DNP-calculated properties were examined and compared to the VASP reference properties with the same initial structures to determine the overall accuracy and precision of the potential. At least two training iterations (iterations 0 and 1) were performed for every element to hone the DNP accuracy.

**2.2.1 Adaptive learning.** All subsequent training iterations beyond the initial dataset (iteration 0) were generated by an “adaptive-learning” (iterations 1, 2, or 3) process utilizing the same initial structures used to create the iteration 0 dataset. We used force-based criteria to select additional configurations (from  $0.07$  to  $2 \text{ eV \AA}^{-1}$ ) to be included in the next iteration of the DNP training utilizing the LAMMPS NVT ensemble approach with the DeePMD-kit, outside of the force tolerance range. We then generated up to ten new DFT structures using VASP NVT to train each structure. Again, as with the validation of “iteration 0”, we verified the DNP accuracy by comparison of the mean of a predicted material property (and the standard deviation of the mean) to the VASP reference value. The process was repeated until the computed cohesive energies ( $E_{\text{coh}}$ ) and per atom volumes were  $\leq 12\%$  of the corresponding DFT reference values (Fig. 2; Table S2†).

### 2.3 DFT reference values

DFT material property references were calculated for the five lattices used as training data sets using VASP parameters similar to the training dataset. For basic lattice properties, such as lattice constants, unit cell volume per atom, and cohesive energy ( $E_{\text{coh}}$ ), we used a conventional primitive unit cell ( $1 \times 1$



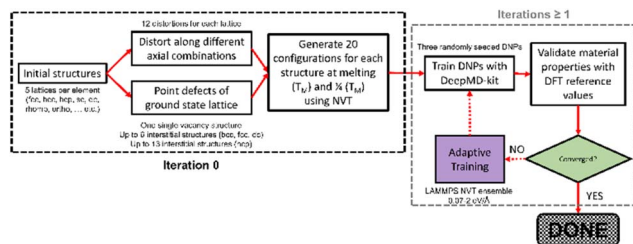


Fig. 2 General training workflow for single-element DNP's.

$\times 1$ ) and previously reported methodologies.<sup>16</sup> We used a  $2 \times 2 \times 2$  supercell for single atom vacancies and interstitial structures.

Elastic constant calculations were made using VASP with the same convergence thresholds,  $2 \times 2 \times 2$  supercell (if the conventional cell contained less than or equal to four atoms), IBRION value of six, and NFREE value of two. All other parameters were the same for the VASP static property calculations, including an energy cut-off of 400 eV. We used a POTMIN value of 0.01 Å for the atomic displacements. Our values generally agree with the elastic constant reported in the MPDB<sup>42</sup> (Table S5†).

## 2.4 LAMMPS calculations

We have detailed descriptions of our process for calculating material properties using LAMMPS and the DNP's reported elsewhere in the literature.<sup>13–16</sup> We used convergence criteria based on  $1 \times 10^{-10}$  eV for energy and forces between minimization steps. A  $4 \times 4 \times 4$  supercell was used for elastic calculations with a 0.005–0.01 Å displacement.

Continuous heating curves for validation are obtained from molecular dynamic simulations employed within an NVT ensemble with one femtosecond timestep. The temperature was controlled using a Berendsen thermostat applied every 100 steps. The temperature was ramped (1 K per femtosecond) from 0 K to approximately 100 K above the experimental melting temperatures, starting with a ground-state lattice supercell relaxed at 0 (bar) pressure. We used  $10 \times 10 \times 10$  supercells for each element's identified ground-state lattice structure. We utilized a compressed version of the DNP for these MD heating simulations, which improved the speed of the simulation with a negligible impact on the accuracy of this calculation.

## 2.5 Validation check on non-trained structures

We assess the transferability of DNP's for each element on structures not explicitly included in the training. Some of the structures were gathered from the MPDB while some were generated<sup>43</sup> by our group. We compared the DNP calculated and averaged cohesive energy ( $E_{\text{coh}}$ ), per atom volume, and elastic constants to the DFT reference values (Tables S8–S10†).

## 2.6 Surface energy calculations

We utilized the LAVA code<sup>44</sup> to calculate low-energy non-reconstructed Miller index surfaces (100), (110), and (111) (fcc,

bcc, and diamond cubic phases and (0001), (10 $\bar{1}0$ ) and (1120) for the hcp phase) surface energies using the LAMMPS wrapper with the DNP's. The average surface energies were determined from the three randomly seeded DNP's and compared to the corresponding DFT (VASP) calculated reference values from the MPDB.<sup>45</sup>

## 3. Results and discussion

We developed a simplistic approach for generating and refining the DFT training dataset for 23 elements (Ag, Al, Au, Co, Cu, Ge, I, Li, Kr, Nb, Ni, Mg, Mo, Os, Pb, Pd, Pt, Re, Sb, Sr, Ti, Zn, and Zr) across the periodic table (Fig. 1) to develop robust DNP's that describe the base material properties for many temperatures, various phases, and selected point defects. The elements chosen in this study represent a wide range of melting temperatures (*e.g.*, Kr and Os), atomic masses (*e.g.*, Li and Pb), electron configurations, elemental groups, and ground state phases ( $11 \times$  fcc,  $6 \times$  hcp,  $2 \times$  bcc,  $1 \times$  diamond cubic,  $1 \times$  tetragonal,  $2 \times$  orthorhombic). Applying these simplified and compact DFT training set criteria to a diverse selection of elements strongly suggests that this general approach applies to most elements on the periodic table for dataset creation, modeling, and refinement for DNP's, at least for single-element systems. We did not investigate the impact of tailoring the model's hyperparameters to each element of the training dataset, which may improve accuracy and performance; instead, we chose to use a “universal” set of parameters for all elements. Our dataset curation focused on achieving good accuracy of lattice constants, cohesive energies, single vacancy defects, interstitial atoms, elastic constants, and thermal stability of the solid phase between 0 K and the melting temperature.

To generate 12 distortions of the lattice in the elastic limit for each lattice of the metal systems, we tested various thresholds from 0.01 to 0.05 Å. We found that the distortion of the lattice by 0.03 Å yielded DNP's that produced the most accurate results overall, with the smallest number of configurations. We ran NVT at the previously defined temperature(s) for each distorted structure to generate 20 configurations. Additionally, we included single vacancy structures for each phase and various self-interstitials (see below) for only the lowest energy phase of each element. In addition to the initial training set, we note that at most, two additional adaptive learning training iterations were required to produce elastic properties that converged with our calculated DFT reference values. The general workflow is depicted in Fig. 2.

As an additional quality check on the precision of the DNP's, while the training improves from iteration to iteration, the standard deviation between the three randomly seeded potentials decreases. We believe this ensemble approach to DNP validation is an important metric to highlight, as we envision these DFT datasets as a minimalistic “core” dataset that can be added to or combined for tailored applications by the community. Reporting the average value and the standard deviation of the values from the three DNP's allows others to assess the precision of the potential and determine whether these values are acceptable for their desired application or if



more training is required. Overall, the maximum number of configurations used for training was less than 6100, with no more than 231 000 total atoms per element (Table S1†).

### 3.1 Basic material properties and phases

We found excellent agreement between the predicted DNP and the DFT reference values for lattice constants and cohesive energies (Fig. 3, Tables S2 and S3†), exemplified by the proximity to the parity line and relatively small standard deviations, as shown in Fig. 2. The percent deviation from the DFT reference values is <12% (excluding Kr with cohesive energies ( $E_{\text{coh}}$ ) < 0.1 eV) per atom volume and <11% for  $E_{\text{coh}}$ . The errors reported in the figures and ESI tables† are the standard deviation of the averaged material property from the three randomly seeded DNP potentials. Notably, we did not include any of these structures in the training data sets; only distorted or defected lattices at temperatures above 0 K were included, yet the

prediction of the DNPs is accurate compared to DFT reference values reflecting its transferability.

### 3.2 Point defects: vacancies and interstitials

Real-world materials are not pristine and contain defects, such as vacancies and interstitials. Therefore, these common point defects were included in the training data sets for each element to improve the basic DNP applicability to real-world materials modeling (Fig. 4 and 6). We compare structures included and excluded in training for single vacancy defect energies (Fig. 4A and Table S4†). The vacancy energies can be relatively small (less than 1 eV), so some structure standard deviations appear more pronounced. Generally, we observe good agreement for most vacancy energies. However, we do not achieve the same accuracy for the energies of the non-defected ground state lattices exemplified in Fig. 3.

For the self-interstitial facilities, we examine a large variety of tetrahedral ( $T_d$ ), octahedral ( $O_h$ ), dumbbell (db), and crowdion

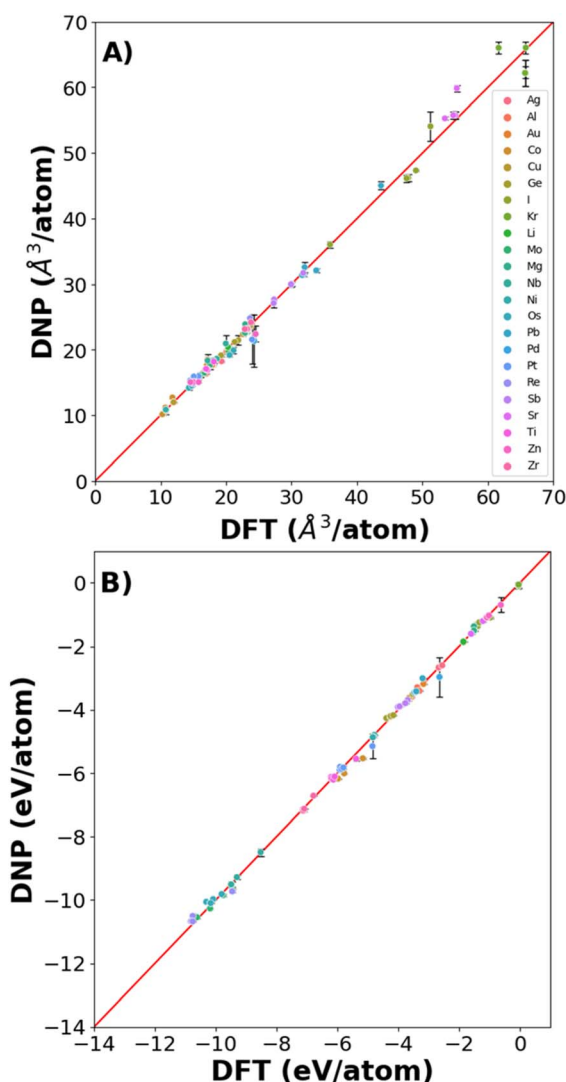


Fig. 3 Parity plot of (A) cell volume/atom and (B) cohesive energies for all elements and phases.

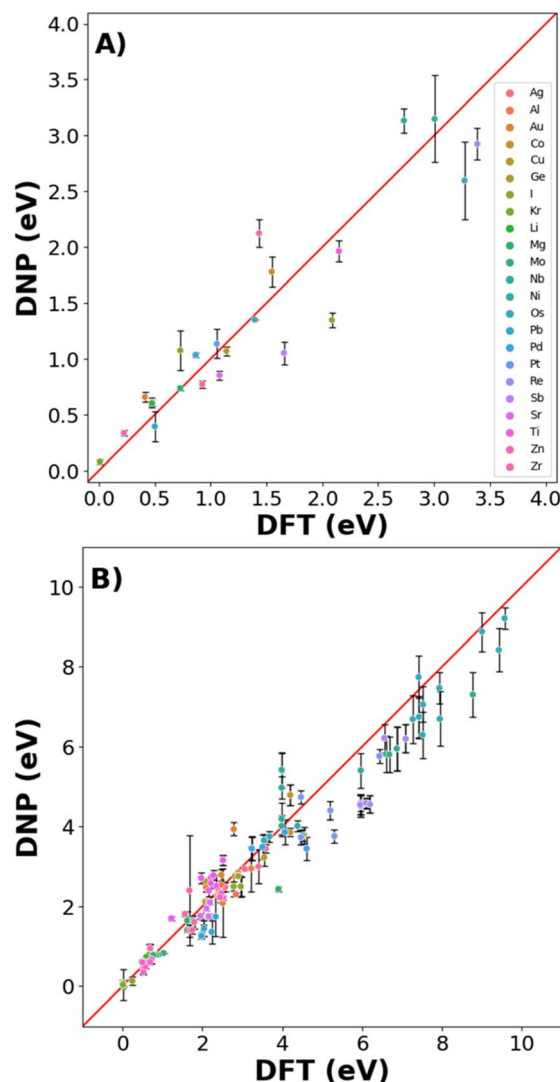


Fig. 4 Parity plot of point defects (A) vacancies (B) single self-interstitial atom energies.





for the lowest energy/ground state phase for each element provided the phase was bcc,<sup>46</sup> fcc,<sup>16</sup> diamond cubic,<sup>47</sup> or hcp<sup>48</sup> (Fig. 4B and Table S5†). We observe good agreement between the average DNP value and the calculated DFT value; however, we note that few interstitials exhibit significant standard deviations of the mean. Upon closer scrutiny, the corresponding interstitials were deemed unstable, as the initial and final structures exhibited an unusual change in the cell volume in the DFT reference calculations; therefore, they were omitted from the validation (Fig. 4 and Table S5†).

### 3.3 Elastic constants

Generating DNPs that accurately predict elastic constants for multiple lattice phases per element is challenging, given that this relies on finite differences. This has not been frequently reported in the literature.<sup>19,49</sup> Fig. 5 compares the DNP and DFT calculation results for unique elastic constants ( $C_{11}$ ,  $C_{12}$ ,  $C_{13}$ ,  $C_{22}$ ,  $C_{33}$ ,  $C_{44}$ ,  $C_{55}$ , and  $C_{66}$ ) for each element's ground state phase (Table S6†). DFT calculations of elastic constants can be highly sensitive to cut-off energies, k-grid spacings, and supercell size.<sup>13</sup> We observe a more significant standard deviation for the elements with heavier nuclei and unfilled electron shells (e.g., Os and Re). Therefore, the observed standard deviations scale with the magnitude of the average value of the elastic constant.

**3.3.1 Summary.** We summarize our training validation results illustrated in Table S7,† which highlights the % deviations of the DNP from that of the DFT reference values (Tables S2 and S4–S6,† and Fig. 3–5) for each parameter class. Generally, the average error in the per atom volume and  $E_{\text{coh}}$  are less than 5%, excluding Krypton (Tables S2 and S7†) which has relatively small  $E_{\text{coh}}$  ( $\sim 0.04$ – $0.08$  eV). Similarly, we observe a trend of larger % deviations point defect energies increases. However, the %  $E_{\text{coh}}$  for these point defect structures is less than 10% (excluding Kr) from the DFT reference. Minor deviations from the DFT reference value 0.01–0.02 eV in both the

pristine and defected can lead to significant errors in the calculated defect energy. Elastic constants are  $\leq 25\%$  in error for most elements on average. However, we observe, on average, larger discrepancies for Pb, Re, Sb, Ti, Zn, and Zr (Table S7†). These deviations can be further reduced with additional training focused on these structures. Overall, the observed variations are similar to Zuo *et al.*<sup>27</sup> report for multiple MLP models. We note, however, that Zuo *et al.* trained on a single lattice phase, and the transferability of the MLPs was not thoroughly explored.

**3.3.2 Transferability of DNPs.** The transferability of a DNP reflects its ability to accurately predict structures or property structures that were not included in the training set. Our previous work noted the good transferability of the DNP.<sup>14,15</sup>

Here, we examine transferability by testing a limited number of phases (either from the MPDB or generated) per element and comparing them to DFT reference values.

Fig. 6 shows that the potentials predict the per atom volume (Fig. 6A) and  $E_{\text{coh}}$  (Fig. 6B) well, with only a small number of

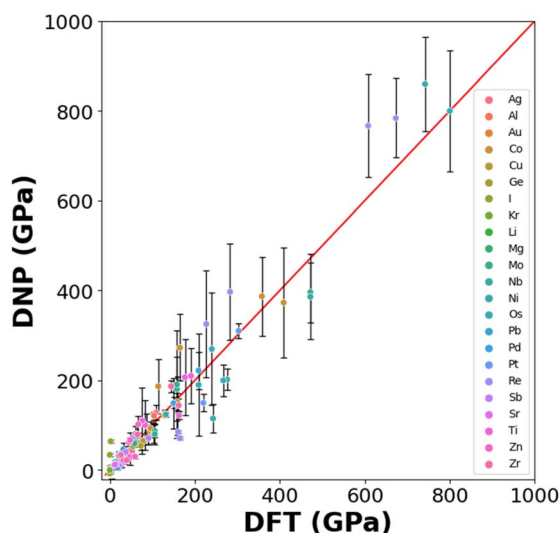


Fig. 5 Calculated DNP and DFT elastic constants.

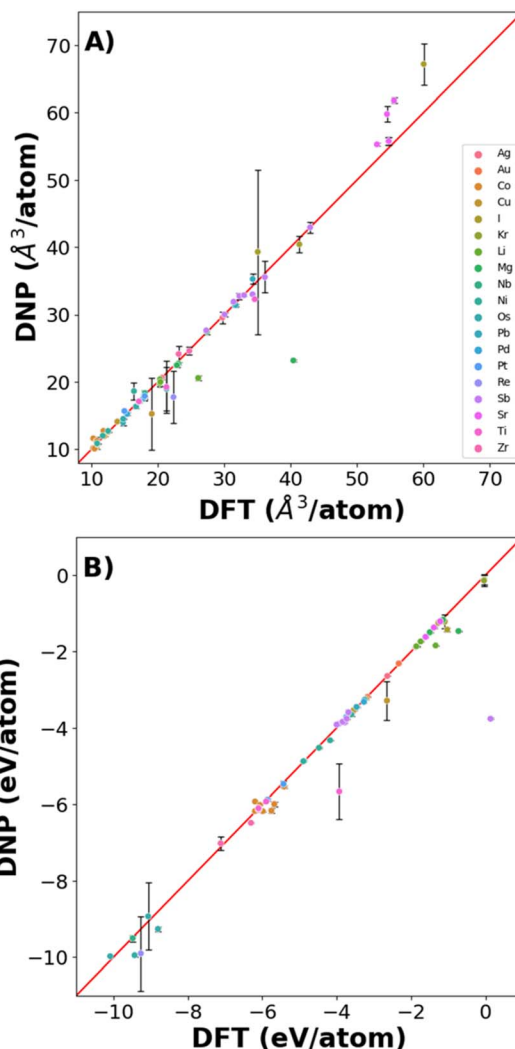


Fig. 6 DNP predictive accuracy for phases not included in the training dataset for (A) volume/atom and (B) cohesive energy.



structures where  $E_{\text{coh}}$  and per atom volumes were poorly predicted (Fig. 6 and Table S9†). However, the % average vacancy energy error (and standard deviation) in the single atom vacancy is more significant than we observed for the trained structures (Tables S4 and S10†), highlighting the boundaries of DNP transferability.

Additionally, comparing the elastic constant for non-ground state phases demonstrates agreement with DFT reference values (Table S8†). Although the agreement is less than desirable for some of these lattices, additional training is necessary to describe the untrained vacancies and non-refined elastic constant predictions. However, the overall transferability of these simple phases and point defects is remarkable. Further, these DNPs can be extended to other properties.

**3.3.3 Surface energies.** Surface energies are essential properties for materials for understanding material growth, adsorbate behavior, and catalytic performance.<sup>50,51</sup> Despite the importance of planar structures, we did not include these in the initial training to reduce the size of the dataset. However, as shown in Fig. 7, the DNPs predict surface energies reasonably well for low Miller index structures (e.g., fcc, bcc, diamond – (001) (011), and (111); or hcp – (0001), (10 $\bar{1}$ 0), and (1120)) (Table S11†). Although further training is required to improve the accuracy of the surface energy predictions, the transferability of these DNPs is surprising, as we have not introduced any aperiodic structures resembling a surface in the training set.

**3.3.4 Thermal stability of the solid phase.** As a final assessment of the robustness of these DNPs, we conducted MD simulations from 0 K to each element's melting temperature (Fig. 8) using an NVT approach and a Benderson thermostat. During the iterative training, we observed poor thermal stability for the elements with relatively high melting temperatures (above 2000 K). This leads us to include an additional group of training data at a temperature of 60% of the melting point.

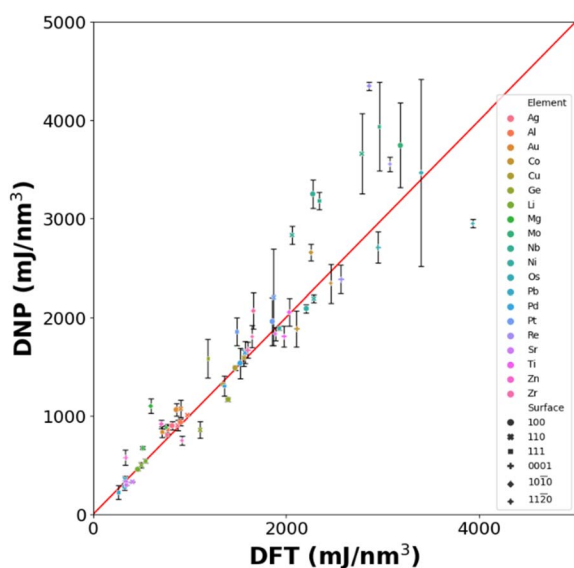


Fig. 7 DNP prediction of low Miller index surfaces (<2) for selected elements compared with DFT reference values. Note that DNPs are trained only on bulk configurations, not surfaces.

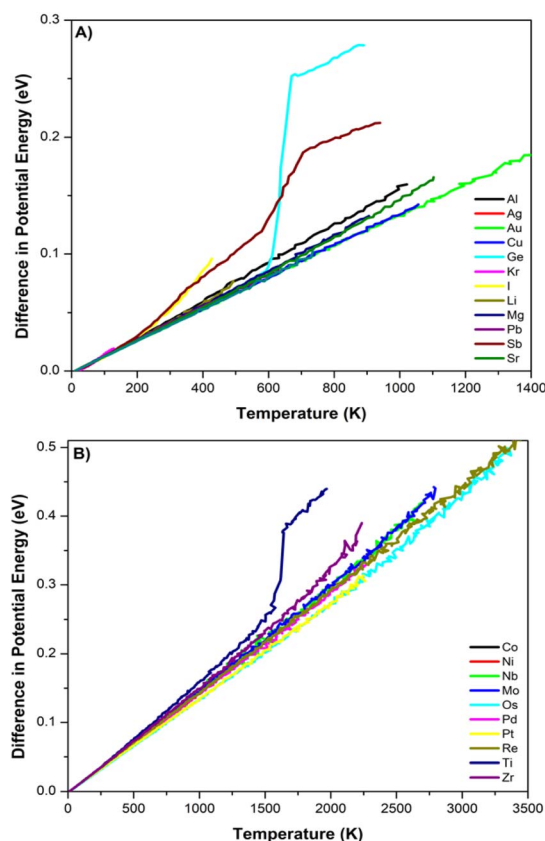


Fig. 8 Potential energy vs. temperatures for all 23 DNPs generated the difference in the potential energy from 0 K for each element with (A) an element with melting temperatures less than 1700 K and (B) an element with melting temperatures over 1700 K.

Including these data vastly improved the solid-state thermal stability up to the melting temperature and improved the initial (iteration 0) predictions of the elastic constants. Even though the training data set included only two temperatures, we found well-behaved heating of these elemental bulk materials with supercells of  $10 \times 10 \times 10$  for each element's ground state configuration. This result is surprising but not wholly unexpected given that the interpolation of the material properties using DNPs has been noted by us<sup>14–16</sup> and others in the literature.<sup>52</sup> We note that the training did not explicitly include structures describing liquid phase behavior. Therefore, we do not expect the phase transition from solid to liquid to be reasonably predicted for all these elemental DNPs. Future investigations focusing on the refinement of modeling solid–liquid phase transitions are the focus of ongoing investigations.

## 4. Conclusions

We have described a general curation methodology by constructing relatively small sets of DFT configurations (<6000) for training single-element atomistic potentials using the DeepMD-kit with a DeepPot-SE approach. Our dataset curation recipe is effective for obtaining a diverse sampling of elements across the periodic table, describing various benchmark material properties



with reasonable fidelity to DFT reference values. Additionally, we estimate the DNP's predictive accuracy range from the three randomized seeded versions to give a baseline range of values before the training sets are modified. Lastly, we found that these compact training sets, along with the DNP training approach, produced highly robust and transferrable potentials that could predict many properties that were not explicitly included in the training data. Ultimately, this study will allow users to augment and build upon these small datasets and/or curation methodologies for their unique scientific queries.

Lastly, we note the various limitations and future extensions of and to this work that would benefit the community. Using these hand-curated systematic training datasets, we focused only on the DeepPot-SE approach and did not assess other MLP models. Such a comparative investigation of MLPs, similar to that of Zuo *et al.*<sup>27</sup> or Morrow *et al.*,<sup>53</sup> would be helpful to the community in assessing the fidelity of the dataset and model combination. We hope this study, particularly the developed and shared datasets, will motivate such extensive comparative studies. Additionally, informative metrics describing the DFT training dataset parameters, such as structural, energies, and forces landscapes, would be beneficial for evaluating and comparing training datasets regardless of the MLP model employed. We deem that these future works will be highly informative for all atomistic potential development and benchmarking going forward.

## Data availability

(1) Data used to generate the main text figures are found in the ESI.†

(2) Due to the large DFT training data file sizes, we have generated Github repository for these resources, which can be located by navigating to this link (<https://github.com/saidigroup/23-Single-Element-DNPs>). In addition, example validation scripts for both LAMMPS and VASP are archived, as well as the final iterations for all three randomly seeded DNPs for each of the 23 elements discussed in this study.

## Author contributions

Christopher M. Andolina: conceptualization, data curation, formal analysis, investigation, methodology, resources, software, validation, visualization, writing – original draft. Wissam A. Saidi: conceptualization, formal analysis, funding acquisition, investigation, methodology, project administration, resources, software, supervision, writing – review & editing. Both authors discussed the results and reviewed the manuscript.

## Conflicts of interest

There are no conflicts to declare.

## Acknowledgements

We are grateful to the U.S. National Science Foundation (Award No. CSSI-2003808). We acknowledge R. Saidi for helping with

Fig. 1. Computational support was provided in part by the University of Pittsburgh Center for Research Computing through the resources provided on the H2P cluster, which is supported by NSF (Award No. OAC-2117681).

## Notes and references

- 1 J. Behler and G. Csányi, *Eur. Phys. J. B*, 2021, **94**, 142, DOI: [10.1140/epjb/s10051-021-00156-1](https://doi.org/10.1140/epjb/s10051-021-00156-1).
- 2 A. M. Miksch, T. Morawietz, J. Kästner, A. Urban and N. Artrith, *Mach. Learn.: Sci. Technol.*, 2021, **2**, 031001, DOI: [10.1088/2632-2153/abfd96](https://doi.org/10.1088/2632-2153/abfd96).
- 3 J. Behler, *J. Chem. Phys.*, 2016, **145**, 170901, DOI: [10.1063/1.4966192](https://doi.org/10.1063/1.4966192).
- 4 Y. Mishin, *Acta Mater.*, 2021, **214**, 116980, DOI: [10.1016/j.actamat.2021.116980](https://doi.org/10.1016/j.actamat.2021.116980).
- 5 Z. Guo, D. Lu, Y. Yan, S. Hu, R. Liu, G. Tan, N. Sun, W. Jiang, L. Liu and Y. Chen, *27th PPoPP*, 2022, pp. 205–218, DOI: [10.1145/3503221.3508425](https://doi.org/10.1145/3503221.3508425).
- 6 J. F. Rodrigues Jr, L. Florea, M. C. F. de Oliveira, D. Diamond and O. N. Oliveira Jr, *Discov. Mater.*, 2021, **1**, 12, DOI: [10.1007/s43939-021-00012-0](https://doi.org/10.1007/s43939-021-00012-0).
- 7 J. Westermayr, S. Chaudhuri, A. Jeindl, O. T. Hofmann and R. J. Maurer, *Digit. Discov.*, 2022, **1**, 463–475, DOI: [10.1039/d2dd00016d](https://doi.org/10.1039/d2dd00016d).
- 8 M. Haghighatdari, J. Li, X. Guan, O. Zhang, A. Das, C. J. Stein, F. Heidar-Zadeh, M. Liu, M. Head-Gordon, L. Bertels, H. Hao, I. Leven and T. Head-Gordon, *Digit. Discov.*, 2022, **1**, 333–343, DOI: [10.1039/d2dd00008c](https://doi.org/10.1039/d2dd00008c).
- 9 V. Zaverkin, D. Holzmüller, I. Steinwart and J. Kästner, *Digit. Disc.*, 2022, **1**, 605–620, DOI: [10.1039/d2dd00034b](https://doi.org/10.1039/d2dd00034b).
- 10 M. J. Burn and P. L. A. Popelier, *Digit. Disc.*, 2023, **2**, 152–164, DOI: [10.1039/d2dd00082b](https://doi.org/10.1039/d2dd00082b).
- 11 L. Ward and C. Wolverton, *Curr. Opin. Solid State Mater. Sci.*, 2017, **21**, 167–176, DOI: [10.1016/j.cossms.2016.07.002](https://doi.org/10.1016/j.cossms.2016.07.002).
- 12 S. Käser, L. I. Vazquez-Salazar, M. Meuwly and K. Töpfer, *Digit. Disc.*, 2023, **2**, 28–58, DOI: [10.1039/d2dd00102k](https://doi.org/10.1039/d2dd00102k).
- 13 D. Bayerl, C. M. Andolina, S. Dwaraknath and W. A. Saidi, *Digit. Disc.*, 2022, **1**, 61–69, DOI: [10.1039/d1dd00005e](https://doi.org/10.1039/d1dd00005e).
- 14 C. M. Andolina, J. G. Wright, N. Das and W. A. Saidi, *Phys. Rev. Mater.*, 2021, **5**, 083804, DOI: [10.1103/PhysRevMaterials.5.083804](https://doi.org/10.1103/PhysRevMaterials.5.083804).
- 15 C. M. Andolina, M. Bon, D. Passerone and W. A. Saidi, *J. Phys. Chem. C*, 2021, **125**, 17438–17447, DOI: [10.1021/acs.jpcc.1c04403](https://doi.org/10.1021/acs.jpcc.1c04403).
- 16 C. M. Andolina, P. Williamson and W. A. Saidi, *J. Chem. Phys.*, 2020, **152**, 154701, DOI: [10.1063/5.0005347](https://doi.org/10.1063/5.0005347).
- 17 W. Chu, W. A. Saidi and O. V. Prezhdo, *ACS Nano*, 2020, **14**, 10608–10615, DOI: [10.1021/acsnano.0c04736](https://doi.org/10.1021/acsnano.0c04736).
- 18 B. Wang, W. Chu, Y. Wu, D. Casanova, W. A. Saidi and O. V. Prezhdo, *J. Phys. Chem. Lett.*, 2022, **13**, 5946–5952, DOI: [10.1021/acs.jpclett.2c01452](https://doi.org/10.1021/acs.jpclett.2c01452).
- 19 P. Wisesa, C. M. Andolina and W. A. Saidi, *J. Phys. Chem. Lett.*, 2023, **14**, 468–475, DOI: [10.1021/acs.jpclett.2c03445](https://doi.org/10.1021/acs.jpclett.2c03445).
- 20 K. Lee, D. Yoo, W. Jeong and S. Han, *Comput. Phys. Commun.*, 2019, **242**, 95–103, DOI: [10.1016/j.cpc.2019.04.014](https://doi.org/10.1016/j.cpc.2019.04.014).



- 21 G. Sivaraman, L. Gallington, A. N. Krishnamoorthy, M. Stan, G. Csányi, Á. Vázquez-Mayagoitia and C. J. Benmore, *Phys. Rev. Lett.*, 2021, **126**, 156002, DOI: [10.1103/PhysRevLett.126.156002](#).
- 22 A. V. Shapeev, *Multiscale Model. Simul.*, 2016, **14**, 1153–1173, DOI: [10.1137/15m1054183](#).
- 23 A. P. Bartók, M. C. Payne, R. Kondor and G. Csányi, *Phys. Rev. Lett.*, 2010, **104**, 136403, DOI: [10.1103/PhysRevLett.104.136403](#).
- 24 K. Choudhary, B. DeCost, C. Chen, A. Jain, F. Tavazza, R. Cohn, C. W. Park, A. Choudhary, A. Agrawal, S. J. L. Billinge, E. Holm, S. P. Ong and C. Wolverton, *npj Comput. Mater.*, 2022, **8**, 59, DOI: [10.1038/s41524-022-00734-6](#).
- 25 A. Y.-T. Wang, R. J. Murdock, S. K. Kauwe, A. O. Oliynyk, A. Gurlo, J. Brgoch, K. A. Persson and T. D. Sparks, *Chem. Mater.*, 2020, **32**, 4954–4965, DOI: [10.1021/acs.chemmater.0c01907](#).
- 26 J. Hill, G. Mulholland, K. Persson, R. Seshadri, C. Wolverton and B. Meredig, *MRS Bull.*, 2016, **41**, 399–409, DOI: [10.1557/mrs.2016.93](#).
- 27 Y. Zuo, C. Chen, X. Li, Z. Deng, Y. Chen, J. Behler, G. Csányi, A. V. Shapeev, A. P. Thompson, M. A. Wood and S. P. Ong, *J. Phys. Chem. A*, 2020, **124**, 731–745, DOI: [10.1021/acs.jpca.9b08723](#).
- 28 D. Zhang, H. Bi, F.-Z. Dai, W. Jiang, L. Zhang and H. Wang, *arXiv*, 2022, preprint, arXiv:2208.08236, DOI: [10.48550/arXiv.2208.08236](#).
- 29 Y. Zhang, H. Wang, W. Chen, J. Zeng, L. Zhang, H. Wang and W. E, *Comput. Phys. Commun.*, 2020, **253**, 107206, DOI: [10.1016/j.cpc.2020.107206](#).
- 30 A. Jain, S. P. Ong, G. Hautier, W. Chen, W. D. Richards, S. Dacek, S. Cholia, D. Gunter, D. Skinner, G. Ceder and K. A. Persson, *APL Mater.*, 2013, **1**, 011002, DOI: [10.1063/1.4812323](#).
- 31 C. Draxl and M. Scheffler, *J. Phys. Mater.*, 2019, **2**, 036001, DOI: [10.1088/2515-7639/ab13bb](#).
- 32 T. Wen, L. Zhang, H. Wang, W. E and D. J. Srolovitz, *Mater. Futures*, 2022, **1**, 022601, DOI: [10.1088/2752-5724/ac681d](#).
- 33 A. Jain, G. Hautier, C. J. Moore, S. Ping Ong, C. C. Fischer, T. Mueller, K. A. Persson and G. Ceder, *Comput. Mater. Sci.*, 2011, **50**, 2295–2310, DOI: [10.1016/j.commatsci.2011.02.023](#).
- 34 P. Hirel, *Comput. Phys. Commun.*, 2015, **197**, 212–219, DOI: [10.1016/j.cpc.2015.07.012](#).
- 35 J. P. Perdew, K. Burke and M. Ernzerhof, *Phys. Rev. Lett.*, 1996, **77**, 3865–3868, DOI: [10.1103/PhysRevLett.77.3865](#).
- 36 P. E. Blochl, *Phys. Rev. B: Condens. Matter Mater. Phys.*, 1994, **50**, 17953–17979, DOI: [10.1103/physrevb.50.17953](#).
- 37 G. Kresse and D. Joubert, *Phys. Rev. B: Condens. Matter Mater. Phys.*, 1999, **59**, 1758.
- 38 A. Jain, G. Hautier, S. P. Ong, C. J. Moore, C. C. Fischer, K. A. Persson and G. Ceder, *Phys. Rev. B: Condens. Matter Mater. Phys.*, 2011, **84**, 045115, DOI: [10.1103/PhysRevB.84.045115](#).
- 39 M. Methfessel and A. T. Paxton, *Phys. Rev. B: Condens. Matter Mater. Phys.*, 1989, **40**, 3616–3621, DOI: [10.1103/physrevb.40.3616](#).
- 40 H. Wang, L. Zhang, J. Han and W. E, *Comput. Phys. Commun.*, 2018, **228**, 178–184, DOI: [10.1016/j.cpc.2018.03.016](#).
- 41 L. Zhang, J. Han, H. Wang, W. A. Saidi and R. Car, *Adv. Neural Inf. Process. Syst.*, 2018, **31**, 4436–4446.
- 42 M. de Jong, W. Chen, T. Angsten, A. Jain, R. Notestine, A. Gamst, M. Sluiter, C. Krishna Ande, S. van der Zwaag, J. J. Plata, C. Toher, S. Curtarolo, G. Ceder, K. A. Persson and M. Asta, *Sci. Data*, 2015, **2**, 150009, DOI: [10.1038/sdata.2015.9](#).
- 43 P. Hirel, *Comput. Phys. Commun.*, 2015, **197**, 212–219, DOI: [10.1016/j.cpc.2015.07.01](#).
- 44 K. Dang, J. Chen, B. Rodgers and S. Fensin, *Comput. Phys. Commun.*, 2023, **286**, 108667.
- 45 A. Jain, S. P. Ong, G. Hautier, W. Chen, W. D. Richards, S. Dacek, S. Cholia, D. Gunter, D. Skinner, G. Ceder and K. A. Persson, *APL Mater.*, 2013, **1**, 011002, DOI: [10.1063/1.4812323](#).
- 46 W. Xu and J. A. Moriarty, *Phys. Rev. B: Condens. Matter Mater. Phys.*, 1996, **54**, 6941–6951, DOI: [10.1103/PhysRevB.54.6941](#).
- 47 L. J. Munro and D. J. Wales, *Phys. Rev. B: Condens. Matter Mater. Phys.*, 1999, **59**, 3969–3980, DOI: [10.1103/PhysRevB.59.3969](#).
- 48 G. Vêrité, C. Domain, C.-C. Fu, P. Gasca, A. Legris and F. Willaime, *Phys. Rev. B: Condens. Matter Mater. Phys.*, 2013, **87**, 134108, DOI: [10.1103/PhysRevB.87.134108](#).
- 49 J. Wu, Y. Zhang, L. Zhang and S. Liu, *Phys. Rev. B*, 2021, **103**, 024108, DOI: [10.1103/PhysRevB.103.024108](#).
- 50 A. V. Ruban, H. L. Skriver and J. K. Nørskov, *Phys. Rev. B: Condens. Matter Mater. Phys.*, 1999, **59**, 15990–16000, DOI: [10.1103/PhysRevB.59.15990](#).
- 51 H. Zhuang, A. J. Tkalych and E. A. Carter, *J. Phys. Chem. C*, 2016, **120**, 23698–23706, DOI: [10.1021/acs.jpcc.6b09687](#).
- 52 R. Chahal, S. Roy, M. Brehm, S. Banerjee, V. Bryantsev and S. T. Lam, *JACS Au*, 2022, **2**, 2693–2702, DOI: [10.1021/jacsau.2c00526](#).
- 53 J. D. Morrow, J. L. A. Gardner and V. L. Deringer, *J. Chem. Phys.*, 2023, **158**, 121501, DOI: [10.1063/5.0139611](#).

